Elastic scattering and total reaction cross section for the ^{7}Be + ^{27}Al system at near-barrier energies

V. Morcelle,[1,2] R. Lichtenthäler,[3] R. Linares,[1] M. C. Morais,[3] V. Guimarães,[3] A. Lépine-Szily,[3] P. R. S. Gomes,[1] J. Lubian,[1] D. R. Mendes Junior,[1] P. N. De Faria,[1,3] A. Barioni,[3,4] L. R. Gasques,[3] J. M. B. Shorto,[5] K. C. C. Pires,[6] J. C. Zamora,[3,7] R. P. Condori,[3] V. Scarduelli,[3] J. J. Kolata,[8] H. Amro,[8,9] F. D. Becchetti,[10] H. Jiang,[10] E. F. Aguilera,[11] D. Lizcano,[11] E. Martinez-Quiroz,[11] and H. Garcia[11]

[1]*Instituto de Física, Universidade Federal Fluminense, Avenida Litoranea s/n, Gragoatá, Niterói, Rio de Janeiro 24210-340, Brazil*
[2]*Universidade Federal de Itajuba, Campus Itabira, 35900-030 Minas Gerais, Brazil*
[3]*Instituto de Física, Universidade de São Paulo, C. P. 66318, 05314-970 São Paulo, SP, Brazil*
[4]*Instituto de Física, Universidade Federal da Bahia, 40210-340 Bahia, Brazil*
[5]*Instituto de Pesquisas Energ'eticas e Nucleares—IPEN, 05508-000 São Paulo, Brazil*
[6]*Universidade Tecnológica Federal do Paraná, Cornélio Procópio—Parana 86300-000, Brazil*
[7]*Technische Universităt Darmstadt, Darmstadt, Germany*
[8]*Department of Physics, University of Notre Dame, Notre Dame, Indiana 46556, USA*
[9]*Henry Ford Hospital, Detroit, Michigan 48202, USA*
[10]*Department of Physics, University of Michigan, Ann Arbor, Michigan 48109-1120, USA*
[11]*Instituto Nacional de Investigaciones Nucleares, A. P. 18-1027, C. P. 11801, Distrito Federal, Mexico*

(Received 6 February 2013; revised manuscript received 24 March 2014; published 24 April 2014)

Elastic scattering angular distributions of the radioactive weakly bound ^{7}Be on ^{27}Al have been measured at energies near the Coulomb barrier. The interaction optical potential is investigated by using different potentials. Total reaction cross sections have also been obtained.

DOI: 10.1103/PhysRevC.89.044611 PACS number(s): 25.70.Bc, 25.70.Mn

I. INTRODUCTION

The investigation of scattering and reaction mechanisms involving light weakly bound nuclei, both stable and radioactive, at near-barrier energies, has been a subject of great interest in the last years [1–4].

Theoretical and experimental works have been devoted to study the effect of the breakup channel on the fusion and total reaction cross sections, the relative importance of the breakup cross section when compared with fusion and direct transfer cross sections, and the energy dependence of the interacting potential in the scattering process, among other topics. Usually the weakly bound nuclei are the projectiles, which may be stable (^{6}Li, ^{7}Li, and ^{9}Be) and radioactive of different types: no halo (^{8}Li, ^{7}Be), neutron halo (^{6,8}He, ^{11}Be, ^{11}Li), and proton halo (^{8}B).

Particularly the behavior of the energy dependence of the optical potential in the elastic scattering has been investigated in recent years. For tightly bound nuclei is well known the phenomenon called threshold anomaly (TA) [5–7], corresponding to a rapid variation of both the real and imaginary parts of the potential when the bombarding energy decreases towards the Coulomb barrier energy. The TA is then characterized by a localized peak in the real part of the potential and a sharp decrease of the imaginary part as the bombarding energy decreases towards the Coulomb barrier. The behavior of the imaginary part of the potential is related with the closing of reaction channels when the energy approaches the Coulomb barrier. When at least one of the colliding nuclei is weakly bound, the breakup channel may become important and it is experimentally verified that this mechanism has an excitation function that does not decrease sharply at energies below the Coulomb barrier, and may lead to the so called breakup threshold anomaly (BTA) [8,9], when the imaginary potential may even increase as the energy decreases near and below the barrier. This behavior has been observed in the energy dependence of optical potentials obtained by fitting the elastic scattering of several systems involving ^{6}Li, ^{6}He, and ^{8}B projectiles.

Experimentally, the investigation of the presence of TA or BTA through the analysis of elastic scattering angular distributions is a very difficult task, since it can only be assessed at near and below barrier energies, where the elastic scattering is predominantly of the Rutherford type, and small deviations from it may only be obtained from very precise measurements.

In the present work we try to contribute to the investigation of the behavior of the interaction optical potential in the scattering of weakly bound nuclei by measuring elastic scattering angular distributions, at near-barrier energies, for the nonhalo radioactive ^{7}Be projectile on the light ^{27}Al target. ^{7}Be breaks up into ^{4}He + ^{3}He, with breakup threshold energy $S_{\alpha} = 1.58$ MeV. It is the core of the proton-halo ^{8}B nucleus, which breaks up into ^{7}Be + p with threshold energy $S_{p} = 0.138$ MeV and can supply valuable information of astrophysical interest, especially related to its production rate. It is also particularly interesting to compare the behavior of the ^{7}Be scattering and reaction cross sections with those for the stable weakly bound nuclei:

(i) ^{7}Li is its mirror nucleus, it has breakup (α + t) threshold energy of 2.47 MeV and one bound excited state at 0.478 MeV.
(ii) ^{9}Be is its stable isotope with breakup (^{8}Be + n) threshold energy of 1.67 MeV and no bound excited state.
(iii) ^{6}Li has a similar breakup ($\alpha + d$) threshold energy of 1.48 MeV and also no bound excited state.

So far, one knows that the total reaction cross sections for the three stable weakly bound nuclei with the ^{27}Al target are enhanced when compared with tightly bound projectiles and the same target [10].

In Sec. II of this paper we give experimental details. In Sec. III optical model analysis of the measured elastic scattering angular distributions is presented in order to study the energy dependence of the interaction potential at near-barrier energies. The derived reaction cross sections are compared with other systems in Sec. IV. Finally, we mention some conclusions in Sec. V.

II. EXPERIMENTAL SETUP

The ^{7}Be + ^{27}Al elastic scattering experiments have been performed using the RIBRAS [11] and TwinSol [12] radioactive ion beam facilities (RIB) installed respectively at the Nuclear Physics Open Laboratory (LAFN) of the University of São Paulo and the Nuclear Structure Laboratory (NSL) of the University of Notre Dame, USA. The two systems are very similar and the difference between the experiments is that measurements in the RIBRAS system have been performed using the intermediate scattering chamber between the two solenoids whereas in the Twinsol experiment, the scattering chamber after the second solenoid was used. In both cases, the ^{7}Be secondary beam is produced by the one-proton transfer reaction ^{3}He (^{6}Li, ^{7}Be). A ^{3}He gas cell production target is bombarded by a ^{6}Li^{3+} primary beam. Except for the 17.2-MeV experiment, performed at RIBRAS, all other measurements have been performed using ^{8}B as the leading beam, namely, the solenoid current has been adjusted for the magnetic rigidity of ^{8}B produced by the ^{3}He (^{6}Li, ^{8}B) reaction and the ^{7}Be, ^{6}Li, and the α peaks seen in the spectra are part of the cocktail beam of particles with the same magnetic rigidity, accepted by the solenoids. The ^{8}B analysis is underway. ^{27}Al and ^{197}Au secondary targets have been used in both experiments, the latter for normalization purposes, since the scattering of ^{7}Be by the gold target is pure Rutherford in the energy range of the experiments. The nominal Coulomb barrier for the ^{7}Be + ^{27}Al system, calculated by the São Paulo potential [13], is 8.3 MeV in the center-of-mass reference system, corresponding to 10.5 MeV in the laboratory system.

A. RIBRAS

The measurements at RIBRAS have been performed using ^{7}Be secondary beams produced with energies $E_{\rm lab} = 12.3$ and 17.2 MeV (see Table I). Although only one of the two solenoids of this system has been used to select the beam, several experiments have been successfully performed previously; see Refs. [10,14–19]. The ^{6}Li^{3+} primary beam was produced and accelerated in the 8-UD Pelletron Tandem of the University of São Paulo with $E_{\rm lab} = 22.0$ and 27.3 MeV and intensity of 300 nAe. The primary target consists of a gas cell with a length of 3.6 cm with entrance and exit windows of 2.2 μm Havar filled with ^{3}He gas at 1 atm. A Faraday cup after the primary target suppresses the primary beam and measures its intensity by current integration during each run. The secondary beam consists of a cocktail of α, ^{6}Li, ^{7}Be, and ^{8}B particles. The

TABLE I. Summary of ^{7}Be energies and ^{27}Al target thickness for this work.

^{7}Be beam energy (MeV)				^{27}Al target	Laboratory
Equivalent energy	incident	outgoing	ΔE	thickness (mg/cm^2)	
10.0	12.3	8.2	4.1	2.1	RIBRAS
13.8	15.9	12.1	3.8	2.3	TwinSol
15.2	19.7	11.9	7.8	5.0	TwinSol
15.4	17.2	13.9	3.3	2.1	RIBRAS

^{27}Al and ^{197}Au secondary targets' thickness were of 2.1 and 4.6 mg/cm^2, respectively. The detection setup consisted of $\Delta E - E$ telescopes with thicknesses of 20 and 1000 μm and single silicon E detectors of 1000 μm. The solid angles were limited by collimators placed in front of the detectors and were about 13 msr. The $\Delta E - E$ telescopes were placed at forward angles so that ^{7}Be and ^{8}B particles still had sufficient energy to go through the 20-μm ΔE detector allowing for particle identification of the secondary beam. Once the identification had been performed, we used single E detectors for elastic scattering measurements in an angular range from 15 to 80° in the center-of-mass reference system, with 5.0° steps and an angular resolution of 3.0°. Measurements with the ^{197}Au target were performed before and after the ^{27}Al target runs to check for ^{7}Be production rate in order to guarantee that the secondary beam production was monitored during the data acquisition. The ^{7}Be energies were determined by energy measurements in the detectors, which were calibrated using a ^{241}Am radioactive source.

Figure 1 shows a $\Delta E - E_{\rm residual}$ biparametric spectrum for the scattering of the cocktail of beams on ^{27}Al at the

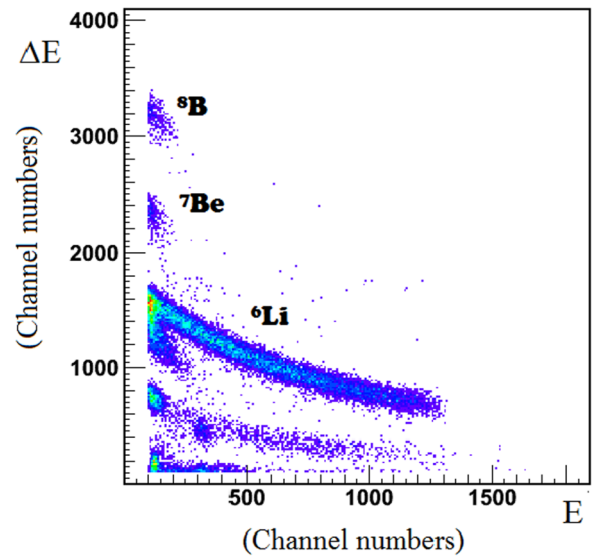

FIG. 1. (Color online) Biparametric spectrum for incident energy $E_{\rm lab}(^{7}\text{Be}) = 12.3$ MeV (10.0 MeV equivalent energy) and $\theta_{\rm lab} = 20°$, obtained in São Paulo (RIBRAS). E is the residual energy in the detector.

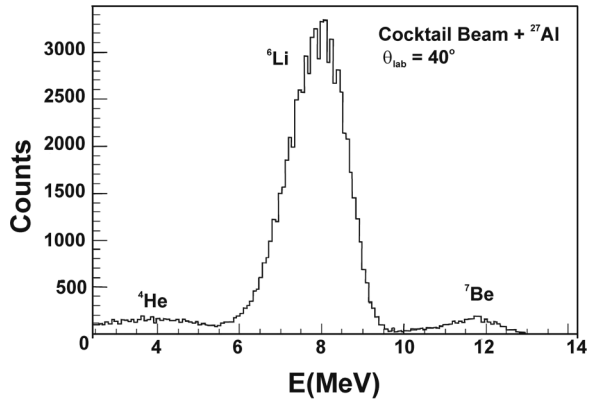

FIG. 2. One-dimensional spectrum for $\theta_{\rm lab} = 40^\circ$ obtained at RIBRAS, where ^{7}Be was the leading beam with incident energy of 17.2 MeV and equivalent energy of 15.4 MeV.

incident energy of $E_{\rm lab}(^7{\rm Be}) = 12.3$ MeV and $\theta_{\rm lab} = 20^\circ$. ^{8}B was the leading beam in this case. ^{7}Be events are clearly distinguishable from ^{6}Li, ^{8}B, and other contaminants. Below the ^{6}Li contour one observes two peaks corresponding to light particle contaminations such as protons, deuterons, tritons (the lowest peak), and α particles. These particles, which are always present in experiments by the in-flight method, are produced in reactions between the ^{6}Li primary beam and the ^{3}He primary target. Usually these light particles have magnetic rigidity higher than $^7{\rm Be}^{3+}$ which generates energy degraded events falling in the $B\rho$ selection band of the solenoid. To wash out such light particles it would be necessary to perform an additional velocity selection. Nevertheless, contaminant peaks are well separated from the ^{7}Be peak and then do not affect our data reduction.

Figure 2 shows a one-dimensional spectrum (single E detector) for the cocktail beam scattered on the ^{27}Al target, where ^{7}Be was the leading beam with incident energy of 17.2 MeV. One can see that the ^{7}Be peak is clearly separated from the ^{6}Li contaminant peaks.

B. TwinSol

The measurements at $E_{\rm lab}(^7{\rm Be}) = 15.9$ and 19.7 MeV incident energies have been performed in the 10-MV Tandem of the Nuclear Structure Laboratory of the University of Notre Dame, associated with the TwinSol system. The ^{7}Be beam corresponds to a contaminant fraction of the ^{8}B leading beam. After the solenoid selection, the ^{7}Be and ^{8}B beams have the same magnetic rigidity (no degrador has been used in between the two solenoids) and it is simple to determine the ^{7}Be initial beam energy. Secondary targets of ^{27}Al 2.3 mg/cm^2 (for $E_{\rm lab} = 15.9$ MeV) and 5.0 mg/cm^2 (for $E_{\rm lab} = 19.7$ MeV) and one ^{197}Au target of 0.985 mg/cm^2 were used. It shall be pointed out that the ^{7}Be energies quoted above are the beam energies before the target. The effect of the target thickness and the energy loss in the target will be discussed in detail in the next subsection.

The averaged intensity of the ^{7}Be beam was about 10^4 pps for a ^{6}Li beam intensity of 350 nAe. The detection setup was composed of four position sensitive detectors ($x - y$ PSD) of 23 × 23 mm placed at fixed angular positions to cover an angular range from 20° to 55°, in the laboratory frame. A single $\Delta E - E$ telescope (20–1000 μm) placed at 15° was used to identify the α, ^{6}Li, ^{7}Be, and ^{8}B particles.

C. Energy loss in the target

An important point that deserves a more detailed discussion is the effect of the energy loss in the target in the present experiment. Some of the targets are rather thick and the beam energy loss represents a considerable amount of the total beam energy. As a consequence, what we are really measuring is a cross section averaged over the energy range of the beam in the target. Considering that the target can be divided in slices dx, the number of counts in the detector due to a given slice is $dN = \frac{N_{\rm beam} dx \Delta\Omega \sigma(E)}{J}$ where $N_{\rm beam}$ stands for the number of beam particles incident in the target, dx is an infinitesimal slice of the target in units of atoms/cm^2, $\Delta\Omega$ is the detector solid angle, and $\sigma(E)$ the differential cross section at the energy E in the middle of the slice. J is the Jacobian factor of the transformation from the laboratory to the center-of-mass system. By integrating the above equation over the target thickness one obtains $N = \frac{N_{\rm beam}\Delta\Omega}{J} \int_{E_0}^{E_1} \sigma(E) \frac{dx}{dE} dE$ where $\frac{dx}{dE}$ is the reciprocal of the beam stopping power and E_0 and E_1 are the energies before and after the target. Using the approximation $\frac{dx}{dE} \approx \frac{\Delta x}{\Delta E}$ one can take this term out of the integral and one sees that $\sigma_{av} = \frac{1}{\Delta E} \int_{E_0}^{E_1} \sigma(E) dE$ is the measured quantity. Taking the Rutherford cross section energy dependence $\sigma(E) \propto \frac{1}{E^2}$ one can easily solve this integral and one sees that there is an equivalent energy such that $\sigma(E_{\rm eq}) = \sigma_{av}$ with $E_{\rm eq} = \sqrt{E_0 E_1}$. The equivalent energy is then given by the geometrical mean of the energies before and after the target. The geometrical mean usually differs from the energy in the middle of the target by a factor that depends on the target thickness. In the present experiment, the worst case is for the 5 mg/cm^2 target where this difference is of about 6%.

Of course, taking the equivalent energy as the geometrical mean of the energies before and after the target is rigorously valid only for pure Rutherford scattering, however, as we are close to the Coulomb barrier, deviations from the Rutherford cross section only contribute to a small correction on the averaged energies and in fact do not affect our results. Nevertheless, we performed Monte Carlo numerical simulations using realistic optical potentials and the results for the equivalent energies are very similar, within a few percent, to the ones obtained using the above expression.

From now on, all the theoretical analysis in this paper will be performed at the equivalent energies as defined above.

In Table I we summarize all four experimental setups regarding incident energies, equivalent energies, and ^{27}Al target thickness.

D. The angular distributions

The elastic scattering angular distributions are shown in Fig. 3. They have been determined using Eq. (1) given below, where the ^{7}Be + ^{27}Al cross sections are normalized by the Rutherford scattering of ^{7}Be by ^{197}Au at a proper energy, independently of solid angle of the detectors. The error bars

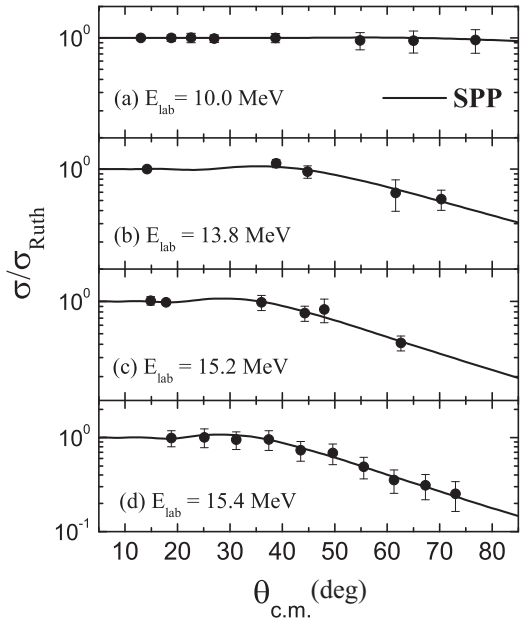

FIG. 3. Fits of the elastic scattering angular distributions using the São Paulo potential.

are essentially due to statistical countings,

$$\left(\frac{\sigma}{\sigma_R}\right)^{x}_{c.m.} = \frac{N_c^x}{N_c^{Au}} \frac{N_{\rm inc}^{Au}}{N_{\rm inc}^x} \frac{J^x}{J^{Au}} \frac{N_a^{Au}}{N_a^x} \frac{\sigma_R^{Au}}{\sigma_R^x}. \quad (1)$$

In Eq. (1), x stands for the ^{27}Al target, N_c is the elastic peak integral (^{27}Al or ^{197}Au), $N_{\rm inc}$ is the number of incident ^{7}Be particles during the run, J is the Jacobian to transform from laboratory to center-of-mass frames, and N_a is the density of the secondary target in atoms/cm^2. The ratio $\frac{N_{\rm inc}^{Au}}{N_{\rm inc}^x}$ is taken as equal to the ratio of the primary beam integrated flux respectively with the gold and aluminum target runs. The primary beam flux is integrated during each run by a Faraday cup placed just after the primary target (see for instance [14]). The ideal situation would be to have aluminum and gold in the same target, to allow an on-line run normalization. However, in experiments using secondary beams by the in-flight method, usually the experimental energy resolution is not sufficient to separate the aluminum and gold peaks, mainly at forward angles where the present measurements have been performed.

Actually the detector energy resolution does not allow us to separate contributions, in the elastic peak, coming from the excitations of the low lying states of the projectile and target (inelastic scattering). To assess the effect of inelastic on the elastic channel we performed coupled channel calculations including the first excited state of the projectile ($1/2^-$ at 0.429 MeV) and the first two excited states of the target ($1/2^+$ and $3/2^+$ at 0.844 and 1.014 MeV). Our calculations indicate that the effect of those inelastic contributions are rather small and can be neglected in the present measurements. The largest contribution was for the most backward angle and for the highest energy (15.4 MeV), and is of about 3% .For this reason we will consider our data as pure elastic angular distributions in what follows.

III. OPTICAL MODEL ANALYSIS OF ELASTIC SCATTERING ANGULAR DISTRIBUTIONS

In this section we present the analysis of the experimental elastic scattering angular distributions. We use two different kinds of potentials, in order to check the consistency of results that should be model independent. In Sec. III A we describe the analysis performed by using the double-folding São Paulo potential (SPP) [13]. The second analysis (Sec. III B) uses a phenomenological Woods-Saxon form factor for the interaction potential. Both analyses were performed using the FRESCO code [20].

A. Analysis using the double-folding São Paulo potential

The São Paulo potential (SPP) [13] is an optical potential which has been successfully used to describe a large variety of systems in a wide energy range, including fusion excitation functions, barrier distributions, and elastic scattering of several weakly bound systems. The energy dependence of the bare interaction arises from the use of a local equivalent model based on the nonlocal nature of the interaction. Within a limited range of energy, as in the present work, it can be considered simply as a double-folding potential based on an extensive systematization of nuclear densities extracted from elastic scattering data and Dirac-Hartree-Bogoliubov calculations. In the present work it is assumed that the imaginary part of the interaction has the same shape as the real part. The data fit procedure is performed with only two free parameters, the normalization factors (strengths) for the real and imaginary parts, N_R and N_I. The best fits of the elastic scattering angular distributions are shown in Fig. 3.

The normalization parameters obtained from the best fits for each energy are shown in Table II, together with the corresponding total reaction cross sections. A χ^2 analysis did not provide a reliable estimation for the errors of the normalization factors mainly due to the large error bars of the experimental data and the small number of points in the angular distributions. Alternatively, the errors on the normalization parameters have been estimated from different calculations in which N_R and N_I were varied to produce equally good fits within the error bars of the experimental data. With this procedure, at least 15 acceptable values of N_R and N_I have been obtained for each energy and their average and standard deviation have been calculated and are presented in Table II.

It is quite clear from Table II that the errors of the normalization factors are huge and do not allow any conclusion about

TABLE II. Values of the strengths of the real and imaginary parts of the São Paulo potential which fit the elastic scattering angular distributions, and the derived total reaction cross sections.

$E_{\rm lab}$ (MeV)	$E_{c.m.}$ (MeV)	N_R	N_I	$\sigma_{\rm reac}$ (mb)
10.0	7.9	$1.0^{+2.8}_{-1.0}$	$1.5^{+2.0}_{-1.5}$	171 ± 92
13.8	11.0	1.3 ± 0.9	1.5 ± 1.0	737 ± 81
15.2	12.1	1.6 ± 0.8	0.9 ± 0.8	951 ± 70
15.4	12.2	1.3 ± 1.0	1.0 ± 0.9	998 ± 74

the energy dependence of the optical potential. Basically all results are consistent with $N_R = N_I = 1$ which corresponds to the standard São Paulo potential.

However, the error bars in the total reaction cross section obtained from this analysis are much smaller and permit a comparison with other systems which will be presented in the next sections.

B. Analysis using the phenomenological Woods-Saxon potential

As a second approach for the fit of the elastic scattering angular distribution data, we use the phenomenological Woods-Saxon potential. The optical model potential $U(r)$ used to derive the elastic scattering differential cross sections is given by the following equation:

$$U(r) = V_{\rm Coul}(r) - V_0 f(r,R_r,a_r) - i W_o f(r,R_i,a_i), \qquad (2)$$

where $V_{\rm Coul}$ is the Coulomb potential of a uniformly charged sphere of radius $R_C = 1.25(A_p^{1/3} + A_t^{1/3})$ fm, A_p and A_t are the mass numbers of the projectile and target respectively; f represents the Woods-Saxon form function which is given by

$$f(r,R,a) = \frac{1}{1+\exp\frac{r-R}{a}}, \qquad (3)$$

where R is the radius and a is the diffuseness; $r_{i,r}$ are the reduced radii, defined as $R_{i,r} = r_{i,r}(A_p^{1/3} + A_t^{1/3})$. The second term of the right side of Eq. (2) is the real part of the potential, where V_0 is its depth. The following term is the volume imaginary potential of the optical potential, where W_0 is its depth.

Several families of optical potential parameters can describe the angular distributions equally well. This is a very well known characteristic of fits with Woods-Saxon potentials. To reduce the ambiguities, we determined the radii of sensitivity R_V and R_W, corresponding to the real and imaginary radii where different potentials have the same value. We let the diffuseness values of the real and imaginary potentials vary from 0.6 to 0.8 fm in steps of 0.05 fm to derive the radii of sensitivity for each energy. Figures 4(a) and 4(b) show families of potentials, which give similar fits, and the derivation of the real and imaginary sensitivity radii, respectively for 13.8 MeV. The derived mean sensitivity radii for the energies investigated are $R_V = 9.10 \pm 0.18$ fm and $R_W = 9.22 \pm 0.61$ fm. Those results are shown in Table III, together with the values found for the ^{6}Li + ^{27}Al [21] and ^{7}Li +^{27}Al [22] systems.

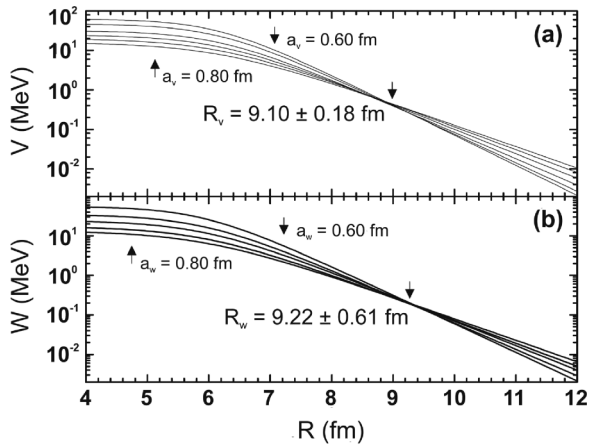

FIG. 4. Derivation of the real (a) and imaginary (b) radius of sensitivity for $E_{\rm lab} = 13.8$ MeV.

TABLE III. Mean radii of sensitivity (in the studied energy interval) for three weakly bound systems with the ^{27}Al target, and the average sensitivity radii R_S (between the mean real and imaginary radii) for the same systems.

System	R_V (fm)	R_W (fm)	R_S (fm)
^{6}Li + ^{27}Al	8.70 ± 0.30	9.61 ± 0.30	9.20 ± 0.42
^{7}Li + ^{27}Al	8.50 ± 0.13	8.50 ± 0.13	8.50 ± 0.18
^{7}Be + ^{27}Al	9.10 ± 0.18	9.22 ± 0.61	9.16 ± 0.63

With an average sensitive radius $R_S = 9.16$ fm (average between R_V and R_W), we performed the usual procedure of starting the fit by keeping fixed all reduced radii and diffuseness parameters, and changing only the real and imaginary depths of the potential. The real and imaginary reduced radii and diffuseness were fixed as $r_r = 1.25$ fm, $a_r = 0.57$ fm, $r_i = 1.20$ fm and $a_i = 0.70$ fm, respectively. The initial values of the real and imaginary depths were $V_0 = 35$ MeV and $W_0 = 18$ MeV, respectively. Good fits of the elastic scattering angular distribution data were obtained, similar to the ones shown in Fig. 3 for the SPP, and will not be shown here. For this reason we did not perform extra fits for the reduced radii and diffuseness. In a procedure similar to the one used with the SPP analysis, different calculations varying the R_s value within its uncertainty were used to estimate the uncertainties on the real and imaginary depths. The values of these depths as a function of energy, the real and imaginary potentials at the average sensitive radius and the total reaction cross sections are shown in Table IV. The energy dependence of the real and imaginary potentials at R_s is shown in Fig. 5. One can observe that the real and imaginary parts of the potential have a roughly energy independent behavior, similar to the results obtained previously with the SPP. However, given the error bars, it is difficult to draw any definite conclusion concerning the behavior of the optical model energy dependence in the present case.

A different behavior was verified for the elastic scattering of the ^{7}Be + ^{58}Ni system [23], where it is found that the

TABLE IV. Values of the depths of the real and imaginary parts of the Woods-Saxon potential (in MeV) which fit the elastic scattering data, fixing the reduced radii and diffuseness for each energy (in MeV). The real and imaginary potentials (in MeV) at the average sensitive radius and the reaction cross sections (in mb) are also shown.

$E_{\rm lab}$	V_o	W_o	V_{R_S}	W_{R_S}	$\sigma_{\rm reac}$
10.0	16 ± 15	33 ± 16	$0.09\ ^{+0.17}_{-0.09}$	0.30 ± 0.22	141 ± 56
13.8	62 ± 13	25 ± 10	0.34 ± 0.18	0.23 ± 0.10	741 ± 48
15.2	68 ± 17	21 ± 9	0.37 ± 0.18	0.22 ± 0.09	896 ± 71
15.4	73 ± 14	19 ± 11	0.41 ± 0.18	0.19 ± 0.10	921 ± 98

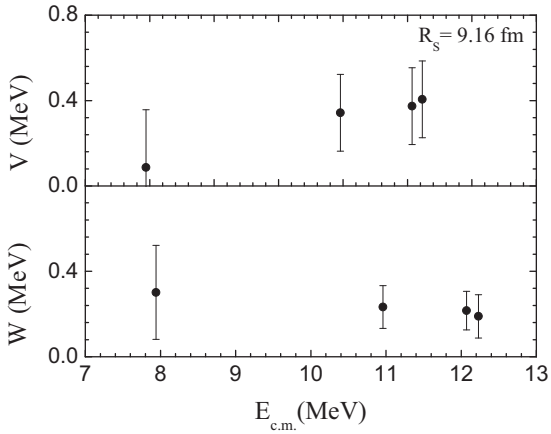

FIG. 5. Energy dependence of the optical potential using the volume Woods-Saxon potential at the average sensitivity radius (see text for details).

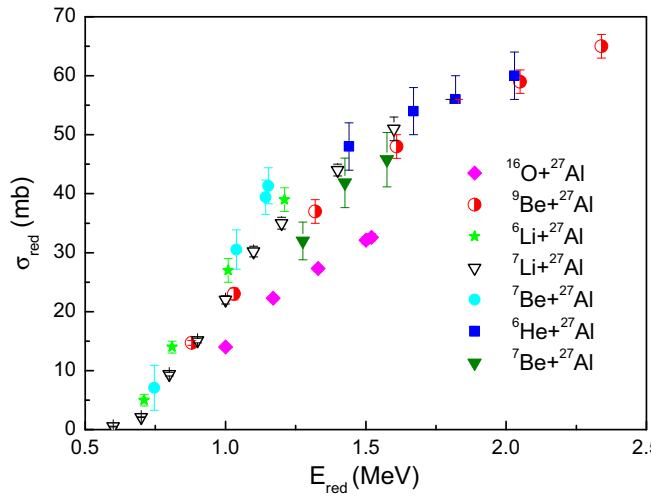

FIG. 6. (Color online) Reduced total reaction cross sections for several projectiles and the same ^{27}Al target, using the reduction procedure proposed in Ref. [25].

imaginary potential increases as the energy decreases towards the barrier energy, with a behavior more compatible with the scattering of ^{6}Li rather than ^{7}Li. However from Table III we can also observe that the average sensitivity radius for ^{7}Be is closer to ^{6}Li than to its mirror ^{7}Li projectiles. These results are in agreement with the studies of Ref. [24] where it was shown, by means of continuum discretized coupled channel calculations for the ^{6,7}Li + ^{208}Pb and ^{7}Be + ^{208}Pb systems, that ^{7}Be with its low breakup threshold behaves like ^{6}Li rather than ^{7}Li.

IV. TOTAL REACTION CROSS SECTIONS

To investigate the effect of the breakup and transfer channels of weakly bound nuclei on the total reaction cross section, the most used approach is to measure elastic scattering angular distributions to derive the total reaction cross sections from the optical model fit of the experimental data. Then, comparison of the total reaction cross sections for those systems with some other weakly and tightly bound systems is done. In Tables II and IV is shown the total reaction cross sections obtained for the ^{7}Be + ^{27}Al system, derived from the optical model fitting of the experimental elastic scattering angular distributions. One can notice that the values of cross sections obtained from the Woods-Saxon potential and from the São Paulo potential are similar, within the error bars.

To compare excitation functions for different reactions in the same plot, a proper normalization method must be used, taking into account trivial factors to correct the cross sections and center-of-mass energies, like different sizes and Coulomb barriers of the systems. A widely used reduction method is the one proposed by Gomes *et al.* [25], which consists in dividing the cross section by $(A_P^{1/3} + A_T^{1/3})^2$ and the center-of-mass energy by $Z_P Z_T/(A_P^{1/3} + A_T^{1/3})$, where A_P (Z_P) and A_T (Z_P) are the mass (charge) of projectile and target, respectively. More recently, Shorto *et al.* [26] proposed an alternative method, also widely used nowadays, based on an extension of the reduction method proposed by Canto *et al.* [27], where fusion functions are analyzed, instead of fusion cross sections. Shorto *et al.* proposed to analyze total reaction functions instead of total reaction cross sections. In the following we use both methods to compare total reaction cross sections (or functions), for several weakly bound systems, obtained from the optical model fit of the experimental elastic scattering angular distributions.

In Fig. 6 we show the reduced total reaction cross sections for the ^{7}Be + ^{27}Al system and also for the stable weakly bound projectiles ^{6,7}Li, ^{9}Be, and the tightly bound ^{16}O with the same ^{27}Al target. Data are from [10,21,22,28,29]. We also show data for the ^{7}Be + ^{27}Al system obtained at higher energies than ours ($E_{\rm lab}$ = 17, 19, and 21 MeV) [30]. The reduction method used was the one proposed in Ref. [25]. This figure is similar to Fig. 3 in Ref. [10]. The error bars for all the systems, except for the ^{7}Be + ^{27}Al, were taken from Ref. [10]. For ^{7}Be + ^{27}Al from Ref. [30] we assumed error bars of the order of 8%, similar to the ones reported by Benjamim for ^{6}He [10].

One can observe that the cross sections for the weakly bound projectiles are similar and larger than those for the tightly bound nucleus ^{16}O. The ^{7}Be projectile produces total reaction cross sections similar to the stable weakly bound nuclei, which have breakup threshold energies of the same order. So, from this figure we conclude that the total reaction cross section increases for weakly bound systems, when the breakup process becomes important and transfer channels also are expected to be more important than for tightly bound systems. However, the reaction cross sections are similar for the halo ^{6}He, the radioactive nonhalo ^{7}Be, and the stable weakly bound ^{6}Li, ^{7}Li, and ^{9}Be, contrary to what is observed for heavier targets, when it is found that the reaction cross section values for halo projectiles are larger than those for stable weakly bound ones [14,17,25,31–37]. This different behavior may be attributed to the small Coulomb field for the light projectiles on the light ^{27}Al target, leading to smaller breakup probability than when heavy targets are involved. The

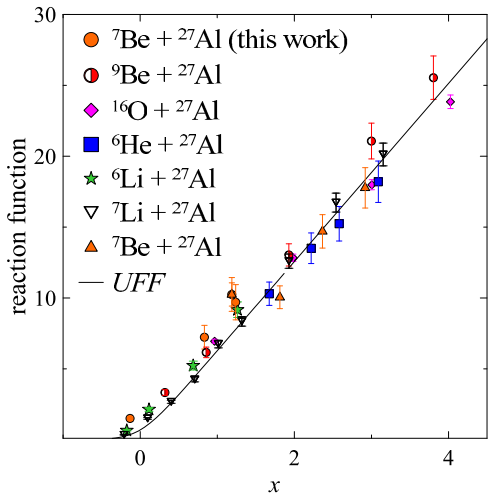

FIG. 7. (Color online) Reduced total reaction cross sections for several projectiles and the same ^{27}Al target, using the reduction procedure proposed in Ref. [26].

same conclusion was reached for the total reaction of ^{7}Be on the light ^{12}C target [18,38].

Figure 7 shows the total reaction functions for the same systems, adopting the reduction prescription proposed by Shorto *et al.* [26]. With this reduction procedure, all systems show the same reaction functions, including the tightly bound ^{16}O. The same behavior was observed in Fig. 1 of Ref. [39], where several systems with the same ^{27}Al target were plotted. Similar behaviors concerning the total reaction functions for heavier targets were obtained; that is, the tightly bound projectiles, heavier than the weakly bound ones, do not show reaction functions smaller than weakly bound ones [14,17,18,26,31,38,39]. Only in Fig. 1 of Ref. [26] is the total reaction cross section of ^{6}He + ^{27}Al higher than those of weakly bound, stable, or tightly bound systems. In the present work we recalculated all total reaction functions and we have found the results shown in Fig. 7, which are in agreement with those of Ref. [39].

The conclusions from both reduction methods concerning the halo and nonhalo weakly bound projectiles are similar, but when one compares with the heavier and tightly bound projectiles, the conclusions are different. Which is the correct way to compare the total reaction cross sections for different systems is still an open question. In the following we will make some comments about this subject.

When one deals with the fusion process, the proper way to reduce cross sections of different systems in the same plot is the method proposed by Canto *et al.* [27], as clearly shown in that reference. In an idealized situation, where channel couplings are not relevant, the fusion cross section near the barrier can be approximated by Wong's formula. In this situation, the reduction method of Ref. [27] produces a system independent function, called UFF. The UFF is then used as a benchmark, so that the deviation of the reduced data with respect to it measures the importance of the couplings. If one aims at understanding the role of breakup couplings, as one usually does when dealing with weakly bound systems, the fusion function is renormalized so that the influence of couplings with bound channels is washed out. The deviation of the renormalized fusion function with respect to its universal form then measures the influence of the breakup channel. In the study of reaction cross sections, the situation is different, mainly when this cross section gets a large contribution from peripheral processes, like inelastic scattering and transfer. The cross section for these processes is associated with surface absorption, which does not correspond to tunneling through the barrier of the bare potential. Thus, the method of Ref. [26] is not expected to work so well. At the present we believe that neither of the two reduction methods discussed in the present paper might be able to fully eliminate all trivial differences among the systems when a broad mass range is considered. However, this is a complex issue that requires further investigation, which is beyond the scope of the present work.

V. CONCLUSIONS

We investigated the elastic scattering of the radioactive no-halo weakly bound ^{7}Be projectile by the light ^{27}Al target, at near-barrier energies. The experiments were performed in two laboratories. The analysis of the energy dependence of the interacting optical potential was performed by two different approaches, the first one using the double-folding Sao Paulo potential and the second one using the phenomenological volume Woods-Saxon potential. From both analyses the potentials that fit the data might be considered as energy independent, although there are large error bars. The conclusions from this energy dependence analysis are susceptible to large uncertainties due to the very thick targets used and to the fact that the data do not cover a sufficiently large angular range.

Furthermore, we compare the behavior of the optical potential for this system with others for weakly bound projectiles (^{6}Li, ^{7}Li, ^{9}Be) and the same target. We did not reach a conclusion about that, since from the energy dependence of the optical potential, the behavior of the scattering of the mirror ^{7}Li seems to be similar to the one of ^{7}Be, whereas the average radii of sensitivity derived for the ^{7}Be and ^{6}Li projectiles are similar. The comparison of the total reaction cross sections for several projectiles on the same ^{27}Al target was investigated by two different widely used methods. Although they were found to be similar for halo and nonhalo weakly bound projectiles from both reduction methods used, the comparison of those systems with the ones with heavier and tightly bound projectiles leads to different conclusions. Which is the proper method to be used is still an open question, and therefore at the present one has to be careful before drawing strong conclusions using one of either methods.

ACKNOWLEDGMENTS

The authors wish to thank CNPq, FAPESP, FAPERJ, PRONEX, and CONACYT for partial financial support. V.M. acknowledges the post-doc junior (PDJ) grant from CNPq/MCTI.

[1] L. F. Canto, P. R. S. Gomes, R. Donangelo, and M. S. Hussein, Phys. Rep. **424**, 1 (2006).
[2] J. F. Liang and C. Signorini, Int. J. Mod. Phys. E **14**, 1121 (2005).
[3] N. Keeley, R. Raabe, N. Alamanos, and J. L. Sida, Prog. Part. Nucl. Sci. **59**, 579 (2007).
[4] O. A. P. Tavares, E. L. Medeiros, and V. Morcelle, Phys. Scr. **82**, 025201 (2010).
[5] M. A. Nagarajan, C. C. Mahaux, and G. R. Satchler, Phys. Rev. Lett. **54**, 1136 (1985).
[6] G. R. Satchler, Phys. Rep. **199**, 147 (1991).
[7] M. E. Brandan and G. R. Satchler, Phys. Rep. **285**, 143 (1997).
[8] P. R. S. Gomes *et al.*, J. Phys. G **31**, S1669 (2005).
[9] M. S. Hussein, P. R. S. Gomes, J. Lubian, and L. C. Chamon, Phys. Rev. C **73**, 044610 (2006).
[10] E. A. Benjamim *et al.*, Phys. Lett. B **647**, 30 (2007).
[11] R. Lichtenthäler *et al.*, Eur. Phys. J. A **25**, s733 (2005).
[12] F. D. Becchetti *et al.*, Nucl. Instrum. Method. A **505**, 377 (2003).
[13] L. C. Chamon, D. Pereira, M. S. Hussein, M. A. CandidoRibeiro, and D. Galetti, Phys. Rev. Lett. **79**, 5218 (1997); Phys. Rev. C **66**, 014610 (2002).
[14] P. N. de Faria *et al.*, Phys. Rev. C **81**, 044605 (2010).
[15] P. N. de Faria *et al.*, Phys. Rev. C **82**, 034602 (2010).
[16] K. C. C. Pires *et al.*, Phys. Rev. C **83**, 064603 (2011).
[17] S. Mukherjee *et al.*, Eur. Phys. J. A **45**, 23 (2010).
[18] J. C. Zamora *et al.*, Phys. Rev. C **84**, 034611 (2011).
[19] A. Barioni *et al.*, Phys. Rev. C **80**, 034617 (2009).
[20] I. J. Thompson, Comput. Phys. Rep. **7**, 3 (1988).
[21] J. M. Figueira *et al.*, Phys. Rev. C **75**, 017602 (2007).
[22] J. M. Figueira *et al.*, Phys. Rev. C **73**, 054603 (2006).
[23] A. Gomez Camacho *et al.*, Nucl. Phys. A **833**, 156 (2010).
[24] N. Keeley, K. W. Kemper, and K. Rusek, Phys. Rev. C **66**, 044605 (2002).
[25] P. R. S. Gomes, J. Lubian, I. Padron, and R. M. Anjos, Phys. Rev. C **71**, 017601 (2005).
[26] J. M. B. Shorto *et al.*, Phys. Lett. B **678**, 77 (2009).
[27] L. F. Canto, P. R. S. Gomes, J. Lubian, L. C. Chamon, and E. Crema, J. Phys. G **36**, 015109 (2009); Nucl. Phys. A **821**, 51 (2009).
[28] P. R. S. Gomes *et al.*, Phys. Rev. C **70**, 054605 (2004).
[29] E. Crema, Master degree thesis, Universidade de São Paulo, 1979.
[30] K. Kalita *et al.*, Phys. Rev. C **73**, 024609 (2006).
[31] N. N. Deshmukh *et al.*, Phys. Rev. C **83**, 024607 (2011).
[32] J. J. Kolata and E. F. Aguilera, Phys. Rev. C **79**, 027603 (2009).
[33] C. Signorini *et al.*, Eur. Phys. J. A **44**, 63 (2010).
[34] E. F. Aguilera *et al.*, Phys. Rev. C **63**, 061603(R) (2001).
[35] E. F. Aguilera *et al.*, Phys. Rev. C **79**, 021601 (2009).
[36] M. Mazzocco *et al.*, Nucl. Phys. A **834**, 488c (2010).
[37] E. F. Aguilera, I. Martel, A. M. Sanchez-Benitez, and L. Acosta, Phys. Rev. C **83**, 021601(R) (2011).
[38] A. Barioni, J. C. Zamora, V. Guimarães, B. Paes, J. Lubian, E. F. Aguilera, J. J. Kolata, A. L. Roberts, F. D. Becchetti, A. Villano, M. Ojaruega, and H. Jiang, Phys. Rev. C **84**, 014603 (2011).
[39] X. P. Yang, G. L. Zhang, and H. Q. Zhang, Phys. Rev. C **87**, 014603 (2013).